

Supplementary Materials for A Boost of Thermoelectric Generation Performance for Polycrystalline InTe by Texture Modulation

Jianghe Feng,[†] Menghui Zhou,[†] Juan Li, Guoying Dong, Shufang Gao,*

Erbiao Min, Chuang Zhang, Jiaqing He,* Rong Sun, Ruiheng Liu*

CONTENTS

1. Modeling of carrier grain boundary scattering

- 1) Trapping state model
- 2) Two-phase model

2. Theoretical calculation

- 1) Theoretical κ_L minimum calculation
- 2) Single parabolic band model
- 3) Kane band model

3. Factors influencing conversion efficiency by COMSOL

- 1) Height of leg
- 2) Section area ratio
- 3) Interface resistance

4. Table and Figures

References

1. Modeling of carrier grain boundary scattering

1) Trapping state model

Based on the assumption that the polycrystalline sample is composed of identical crystallites, the impurity atoms are totally ionized and uniformly distributed, and the GB has negligible thickness compared to the grain size, the expression of σ_{GB} was derived by Seto when GBS is the dominant scattering mechanism:¹

$$\sigma_{\text{GB}} = e^2 d n \left(\frac{1}{2\pi k_B T} \right)^{1/2} \exp \left(\frac{-E_b}{k_B T} \right) \quad (\text{S1})$$

where d is the grain size, k_B the Boltzmann constant, E_b the height of the potential barrier.

The key factor in Equation S2 is E_b , which is expressed as:

$$E_b = \begin{cases} \frac{e^2 d^2 N}{8\varepsilon} & dN < Q_t \\ \frac{e^2 Q_t}{8N\varepsilon} & dN > Q_t \end{cases} \quad (\text{S2})$$

where e is the elementary charge (C), Q_t is the density of trapping states at grain boundaries ($\text{C}\cdot\text{m}^{-2}$) and N is the concentration of ionized impurity atoms (usually dopant atoms, m^{-3}). For TE materials, which in most cases are heavily doped semiconductors, only part of the crystallite is depleted, and the E_b can be described using the formula with $dN > Q_t$. E_b can be obtained from the experimentally measured $\sigma(T)$ when GBS occupies the dominant scattering mechanism of the material.² One can rewrite Equation S1 as:

$$\ln(\sigma T^{-1/2}) = \frac{-E_b}{k_B T} + \text{constant} \quad (\text{S3})$$

Thus, the E_b of all sample was obtained by making the $\ln(\sigma T^{1/2}) - 1/k_B T$ plot, as shown in Fig. S4.

2) Two-phase model

It is worth noting that the σ of <50-HP and 50-HP in 600-773K also undergo the change of main scattering mechanism from GBS to APS with increase of temperature. Based on Matthiessen's rule: $\mu^1 = \mu_{\text{APS}}^{-1} + \mu_{\text{GBS}}^{-1}$, we analyzed the carrier transport mechanism. The main scattering mechanisms are dominated by phonon scattering and grain boundary scattering,^{3,4} respectively, the expressions of σ as

$$\sigma_{\text{AP}} = AT^{-3/2}, \quad \sigma_{\text{GB}} = CT^{-1/2} \exp \left(\frac{-E_b}{k_B T} \right) \quad (\text{S4})$$

The two scattering mechanisms (GBS and APS) coexist in InTe sample in whole temperature range, in order to more accurately expressed σ . Thus, the total σ was written as:

$$\sigma_t^{-1} = \left(AT^{-3/2} \right)^{-1} + \left[CT^{-1/2} \exp\left(\frac{-E_b}{k_B T}\right) \right]^{-1} \quad (\text{S5})$$

It is a simplified formula that can be used to model the experimental σ and the phase fraction here is included in the coefficient A and C , which means that the total resistance was contributed by both the grain and GB parts.

The experimentally measured temperature-dependent electrical conductivities σ for all samples are analyzed using Equation S5. As presented in Fig. S5, the experimental results match well with the calculated curves when considering both the GBS and APS, suggesting the scattering mechanism in TE semiconductor carriers by the combined action of GBS and APS.

In addition, in order to learn more about the two scattering mechanisms of GBS and APS in the material, the temperature exponent r of $\sigma(T)$ could be further derived as:

$$r = \frac{d \ln \sigma}{d \ln T} = \frac{T d \sigma}{\sigma d T} \quad (\text{S6})$$

According to Equation S1 and S2, the $r - T$ plot for all samples is shown in Fig. S3f.

2. Theoretical calculation

1) Theoretical κ_L minimum calculation

The minimum κ_L of InTe was estimated by two different models, termed as Cahill model,⁵ and diffusion model respectively.⁶

Cahill:

$$\kappa_{\text{glass}} \approx 1.21 n^{2/3} k_B \frac{1}{3} (2v_t + v_l) \quad (\text{S7})$$

Diffusion:

$$\kappa_{\text{diff}} \approx 0.76 n^{2/3} k_B \frac{1}{3} (2v_t + v_l) \quad (\text{S8})$$

where n is the number density of atoms, k_B is the Boltzmann constant, v_t is transverse sound velocity, and v_l is the longitudinal sound velocity.

2) Single parabolic band model

Generally speaking, the heavier density of the state effective mass m_d^* favors a larger S . In order to further understand the improvement in S , we calculated m_d^* using the single parabolic

band (SPB) model. According to the Boltzmann transport theory, m_d^* can be calculated by the following equations:

The Seebeck coefficient:

$$S(\eta) = \frac{k_B}{e} \left[\frac{\left(r + \frac{5}{2}\right) F_{\left(r+\frac{3}{2}\right)}(\eta)}{\left(r + \frac{5}{2}\right) F_{\left(r+\frac{1}{2}\right)}(\eta)} - \eta \right] \quad (S9)$$

The Hall carrier concentration:

$$n_H = \frac{1}{eR_H} \frac{(2m_d^* k_B T)^{3/2}}{3\pi^2 \hbar^3} \frac{(r + \frac{3}{2})^2 F_{\left(r+\frac{1}{2}\right)}^2(\eta)}{(2r + \frac{3}{2}) F_{\left(2r+\frac{1}{2}\right)}(\eta)} \quad (S10)$$

Here, $F_{(j)}(\eta) = \int_0^\infty \frac{\xi^j / d\xi}{1 + \exp(\xi + \eta)}$ is the Fermi integral, k_B is the Boltzmann constant, η is the reduced

Fermi level, and $r = -1/2$ when charge carriers are scattered by acoustic phonons, \hbar is the reduced Planck constant, $\xi = E/k_B T$ and $m_d^* = N_V^{2/3} m_b$, m_b is the band effective mass and N_V is the degeneracy of the band valleys.

3) Kane band model

When considering an ellipsoidal Fermi surface involved the ratio of the longitudinal ($m_{||}^*$) to transverse (m_{\perp}^*) effective mass components of the cigar-shaped carrier pocket, the Hall carrier concentration is expressed as:⁷

$$n_H = \frac{1}{eR_H} = A^{-1} \frac{N_V (2m_b^* k_B T)^{\frac{3}{2}}}{3\pi^2 \hbar^3} {}^0F_0^{\frac{3}{2}} \quad (S11)$$

here Hall factor can be written as:

$$A = \frac{3K(K+2)}{(2K+2)^2} {}^0F_{-4}^{\frac{3}{2}} \cdot {}^0F_{-2}^{\frac{3}{2}}, K = m_{||}^* / m_{\perp}^* \quad (S12)$$

and the Seebeck coefficient

$$S = \frac{k_B}{e} \left[\frac{{}^1F_{-2}^{\frac{1}{2}}}{{}^0F_{-2}^{\frac{1}{2}}} - \eta \right] \quad (S13)$$

where ${}^nF_k^m$ has a similar form as the Fermi integral:

$${}^nF_k^m = \int_0^\infty (-\frac{\partial f}{\partial \varepsilon}) \varepsilon^n (\varepsilon + \alpha \varepsilon^2)^m [(1 + 2\alpha\varepsilon)^2 + 2]^{\frac{k}{2}} d\varepsilon \quad (S14)$$

In the above equations, ε is the reduced energy of the electron state, $\alpha (= k_B T/E_g)$ is the reciprocal reduced band separation, f is the Fermi distribution. Because the n_H depends on the K , thus the higher texture degree of (110) for ZM-HP results in the underestimate of the Hall factor, and the relevant overestimate of n_H .

3. Factors influencing conversion efficiency by COMSOL

1) Height of leg

First, we structured the single module, which was consisted of p-type ZM-HP-InTe and commercial n-type $\text{Bi}_2\text{Te}_{2.7}\text{Se}_{0.3}$. The TE performance of the commercial n-type $\text{Bi}_2\text{Te}_{2.7}\text{Se}_{0.3}$ were shown in Fig. S9. And the cross sectional dimensions of p-type InTe and commercial n-type $\text{Bi}_2\text{Te}_{2.7}\text{Se}_{0.3}$ were all $3 \text{ mm} \times 3 \text{ mm}$. The output power and conversion efficiency with increase of the leg height are shown in Fig. S10a and 10c. Due to the internal resistance of TE module constantly increase with increase of the leg height, the output power gradually decrease. Meanwhile, the thermal resistance also increases, as a result, the conversion efficiency gradually increases.

2) Section area ratio

Due to p-type and n-type are thermally parallel structures, the total thermal conduction (κ_{pn}) is $\kappa_{pn}(T) = \kappa_p(T) \frac{A_p}{H} + \kappa_n(T) \frac{A_n}{H}$, the κ_p and κ_n represent the thermal conductivity of p-type and n-type materials, respectively, the A_p and A_n represent the cross-sectional area of p-type and n-type materials, respectively, and the H is the height of the thermoelectric leg. The sum of the cross-sectional areas of p-type and n-type materials is $3 \text{ mm} \times 6 \text{ mm} = 18 \text{ mm}^2$, due to $\kappa_p < \kappa_n$, thus, κ_{pn} decreases with the increasing of A_p/A_n . And p-type and n-type are electrical series, the total resistivity (R_{pn}) is $R_{pn}(T) = \rho(T) \frac{H}{A_p} + \rho_n \frac{H}{A_n}$, the ρ_p and ρ_n represent the resistivity of p-type and n-type materials, the resistance of the TE device first decrease then increase with the ratio of $A = A_p/A_n$ increasing. Thus, the sum of the sectional areas of the fixed n-type and p-type thermal arms is $6 \times 3 = 18 \text{ mm}^2$. The height of thermoelectric legs is fixed at 6.8 mm, one of their sides are fixed at 3 mm, and the other sides are $L_n = 6 / (A + 1) \text{ mm}$ and $L_p = 6 A / (A + 1) \text{ mm}$. In addition, the high temperature end is 573 K, and the low temperature end is 283 K. The simulated current dependence of conversion efficiency and output power under difference ratios of the cross-sectional area of p-type thermal arm to that of n-type are shown in Fig. S10b and d.

3) Contact resistance

According to the simulation results in the first two sections, the sectional area of the n-type thermal arm is set three times larger than that of the p-type thermal arm in order to obtain more high out power and conversion efficiency. Due to size limitation of alumina substrate, the maximum sectional area of the thermal arm is 3×3 mm, we have determined the actual size of the thermoelectric module (p-type : $3 \times 3 \times 6.8$ mm, n-type : $1.7 \times 1.7 \times 6.8$ mm). Because the thermoelectric module has a large resistance (940 m Ω) in practice with the large contact resistance of 580 $\mu\Omega$ cm 2 , the experimental conversion efficiency is lower than the simulated result. When we adjusted the contact resistance to the measurement value with unchanged the internal resistance, the simulated conversion efficiencies (Fig. S11) under different temperature differences (ΔT) of 140 K, 190 K, 240 K and 290 K, when cold side is 283 K, are equivalent to the experimental data. Furthermore, we also predicted the performance if the contact resistance is a normal value of 10 $\mu\Omega$ cm 2 , and the simulated terminal voltages, output powers, and conversion efficiencies are shown in Fig. S11.

Table S1. The thermoelectric properties of related InTe by other reports.

Sample	T (K)	σ (S/cm)	S (μ V/k)	PF (μ W/cmK ²)	κ (W/mK)	zT	κ_L (W/mK)	n_H (10^{19} cm ⁻¹)	μ_H (cm ² V ⁻¹ s ⁻¹)	ref.
InTe	300	54	214	2.47	0.77	0.10	0.73	--	--	
	600	18	274	1.35	0.49	0.17	0.48	--	--	
In_{0.997}Te	300	486	128	7.96	0.68	0.35	0.42	2.8	108.5	8
	600	114	232	6.14	0.42	0.88	0.32	--	--	
InTe	300	169	115	2.24	1.0	0.07	0.92	5.7	18.5	
	700	69	231	3.68	0.49	0.53	0.41	--	--	
In_{0.99}Sb_{0.01}Te	300	121	122	1.80	0.80	0.07	0.73	5.7	13.3	9
	700	91	230	4.81	0.45	0.75	0.36	--	--	
InTe	300	107	118	1.49	0.80	0.06	--	4.3	15.5	
	700	22	209	0.96	0.43	0.16	--	--	--	
In_{0.99}Cu_{0.01}Te	300	87	80	0.56	0.92	0.02	--	6.2	8.8	10
	700	140	182	4.64	0.45	0.70	--	--	--	
In_{0.99}Na_{0.01}Te	300	17	112	0.21	0.74	0.01	--	4.6	2.4	
	700	96	180	3.11	0.41	0.51	--	--	--	
InTe	300	83	94	0.73	--	0.02	0.97	7.8	6.77	
	700	143	188	5.05	--	0.61	0.43	8.5	10.48	
InTe-	300	103	93	0.89	--	0.02	1.09	8.4	6.13	
0.0102CuInTe₂	700	139	193	5.18	--	0.72	0.37	8.8	10.48	

Sample	T (K)	σ (S/cm)	S (μ V/k)	PF (μ W/cmK ²)	κ (W/mK)	zT	κ_L (W/mK)	n_H (10^{19} cm ⁻¹)	μ_H (cm ² V ⁻¹ s ⁻¹)	ref.
InTe	300	115	102	1.20	0.82	0.04	0.75	4.5	15.97	12
	700	96	224	4.82	0.39	0.86	0.28	--	--	
In_{0.999}Pb_{0.001}Te	300	98	85	0.71	0.73	0.03	0.68	6.7	9.14	12
	700	137	194	5.16	0.39	0.93	0.23	--	--	
InTe	300	232	94	2.05	0.80	0.08	--	6.78	21	13
	600	143	195	5.44	0.48	0.68	--	--	--	
InTe_{0.9}	300	99	213	4.49	0.60	0.22	--	1.41	44	13
	600	39	299	3.49	0.40	0.52	--	--	--	
InTe	300	42	105	0.46	0.91	0.02	0.88	4.2	5.3	14
	600	87	160	2.23	0.51	0.26	0.42			
In_{0.98}Cd_{0.02}Te	300	114	125	1.78	0.94	0.06	0.74	6.2	4.4	14
	600	98	207	4.20	0.53	0.48	0.37	--	--	
InTe(001)	300	128	105	1.41	1.19	0.04	--	7.5	--	15
	700	63	178	2.00	--	--	--	--	--	
InTe(110)	300	398	89	3.15	0.72	0.13	0.48	7.5	--	15
	700	185	160	4.74	0.55	0.60	0.33	--	--	
InTe	300	350	127	5.65	0.99	0.17	0.8	3.37	64.9	16
	600	137	221	6.69	0.53	0.76	0.39	2.56	33.4	
In_{0.99}Ga_{0.01}Te	300	382	114	4.96	0.69	0.22	0.47	4.0	59.4	16
	600	185	214	8.47	0.41	1.23	0.23	2.98	38.8	

Sample	T (K)	σ (S/cm)	S (μ V/k)	PF (μ W/cmK ²)	κ (W/mK)	zT	κ_L (W/mK)	n_H (10^{19} cm ⁻¹)	μ_H (cm ² V ⁻¹ s ⁻¹)	ref.
ZM-HP	300	437	140	8.68	0.73	0.36	0.49	4.26	64.2	
	600	123	238	7.04	0.43	0.94	0.30	3.6	21.4	This
<50-HP	300	32	100	0.32	0.65	0.02	0.63	4.8	4.2	work
	600	166	145	3.00	0.53	0.31	0.40	7.1	12.8	

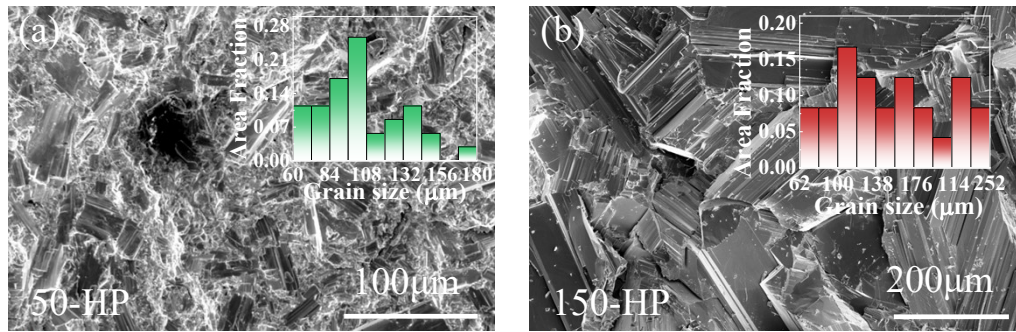


Fig. S1. Cross-section SEM images for the HP InTe samples for (a) 50-HP and (b) 150-HP. The insets are the grain size distributions of 50-HP and 150-HP, respectively.

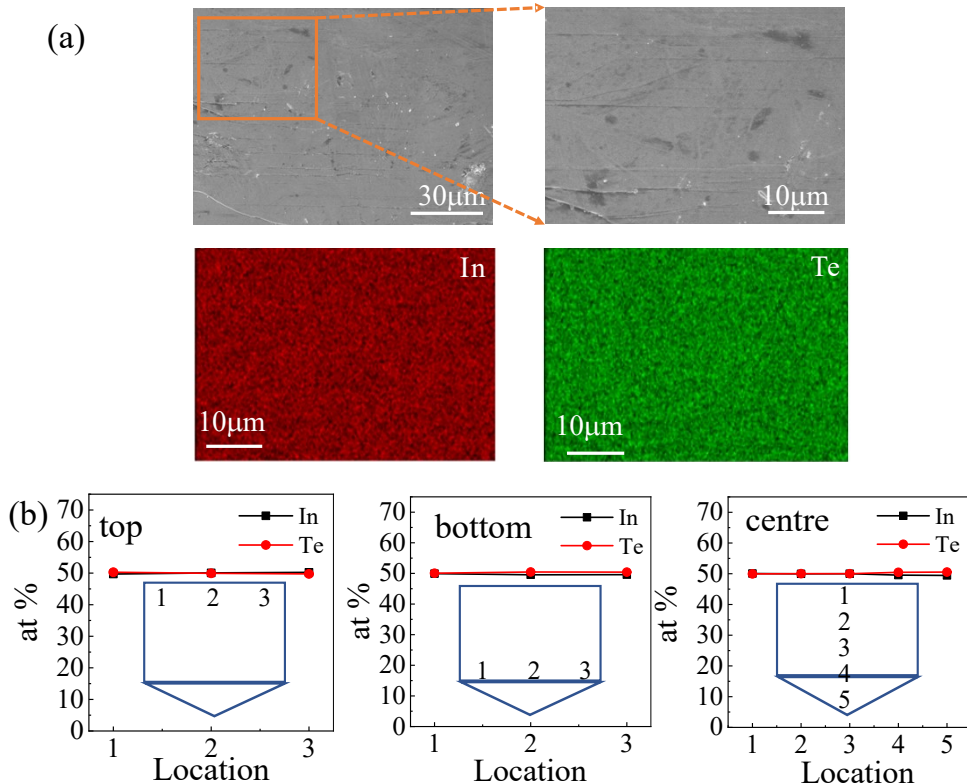


Fig. S2. (a) SEM images and corresponding EDS compositional mappings for the hot-deformed crystal. (b) the atomic ratio of In and Te at different positions of InTe crystal.

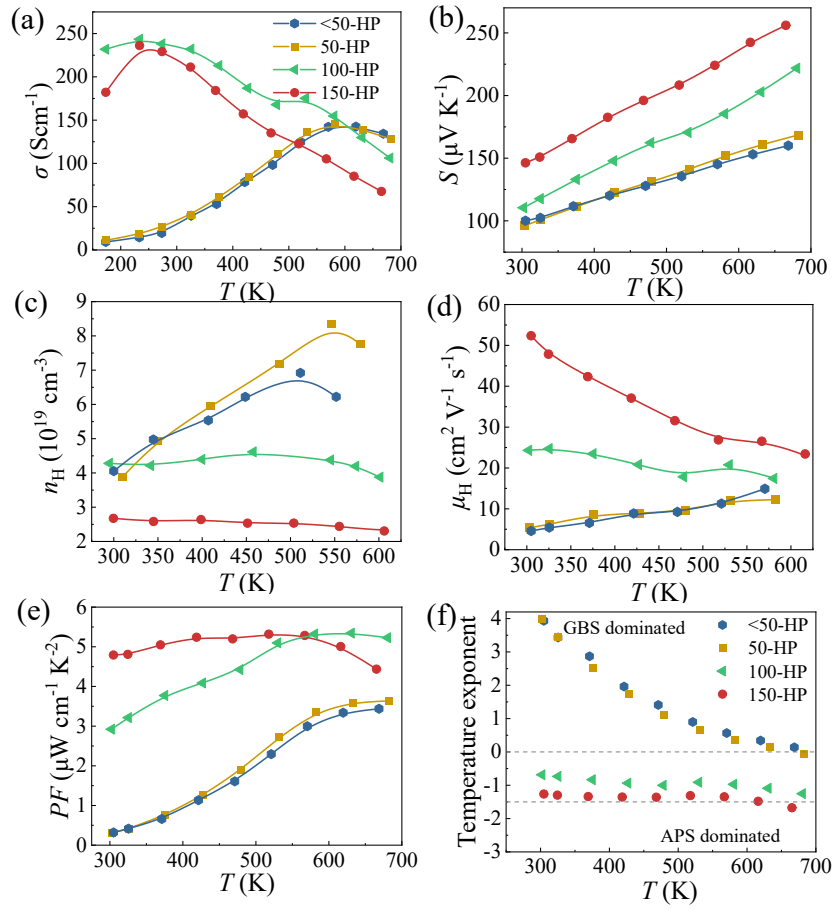


Fig. S3. Temperature dependence of the thermoelectric properties of InTe polycrystalline samples with different particle sizes. (a) Electrical conductivity, (b) Seebeck coefficient, (c) Hall carrier concentration, (d) hall carrier concentration mobility, (e) power factor, and (f) temperature exponent.

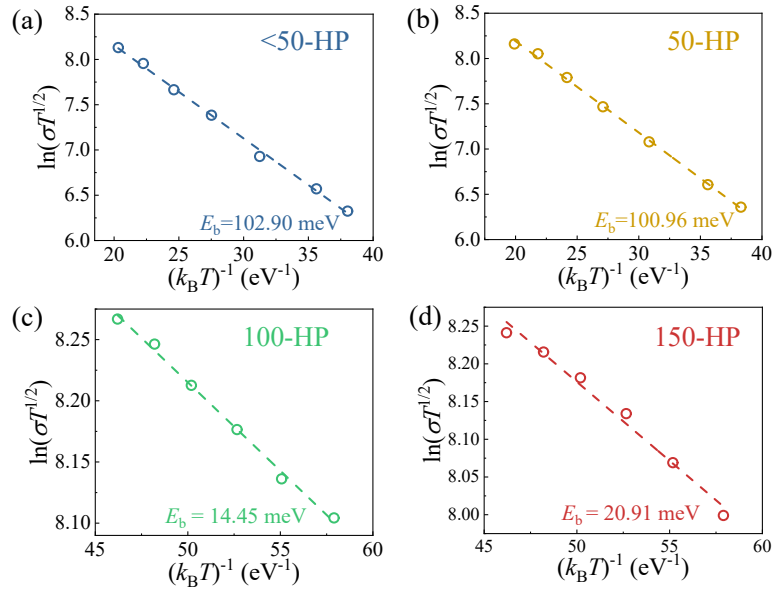


Fig. S4. E_b for the InTe polycrystalline samples. (a) <50-HP, (b) 50-HP, (c) 100-HP and (d) 150-HP.

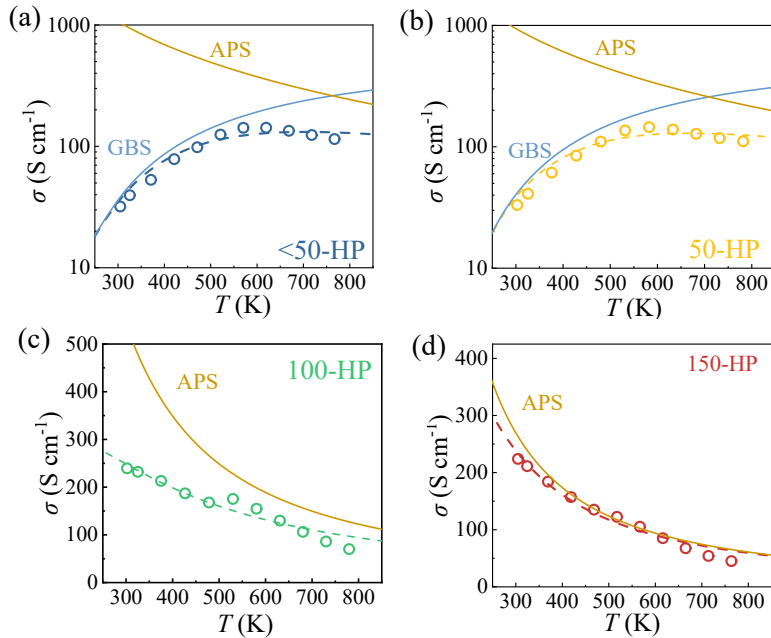


Fig. S5. Temperature dependence of experimental and simulated (by two-phase model) σ for the InTe polycrystalline samples. (a) <50-HP, (b) 50-HP, (c) 100-HP and (d) 150-HP.

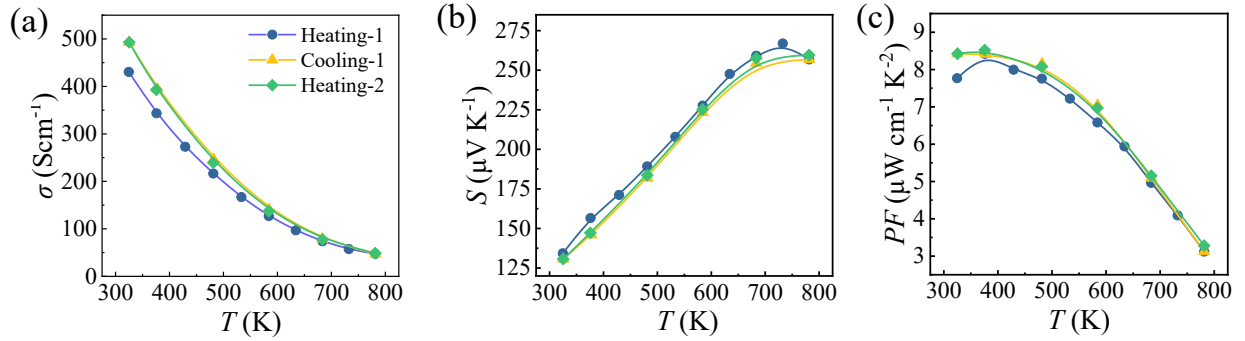


Fig. S6. Temperature dependence of repeat tests of thermoelectric properties for the hot-deformed InTe crystal. (a) Electrical conductivity, (b) Seebeck coefficient and (c) power factor.

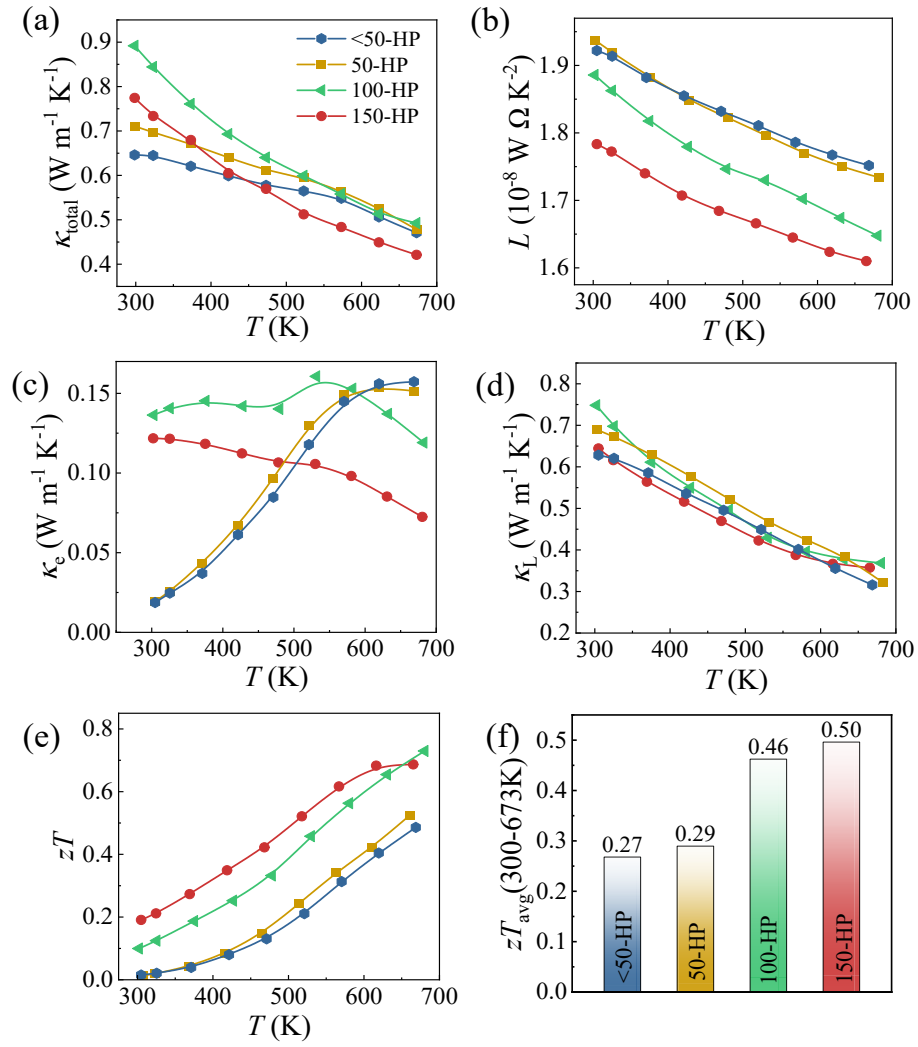


Fig. S7. Temperature dependence of the thermoelectric properties for InTe polycrystalline samples with different grain sizes. (a) Total thermal conductivity, (b) Lorenz number, (c) electron thermal conductivity, (d) lattice thermal conductivity. (e) zT value. (f) The average zT between 300-623K for InTe polycrystalline samples with different grain sizes.

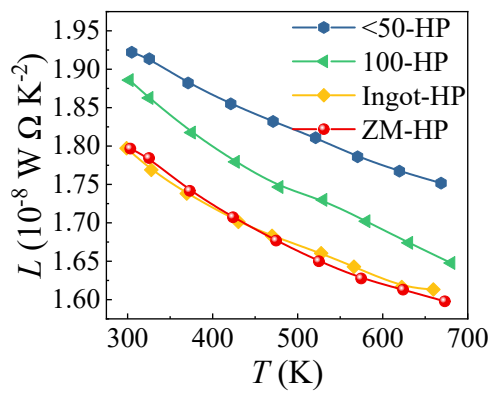


Fig. S8. Temperature dependence of the Lorenz number for InTe polycrystalline samples with different particle sizes.

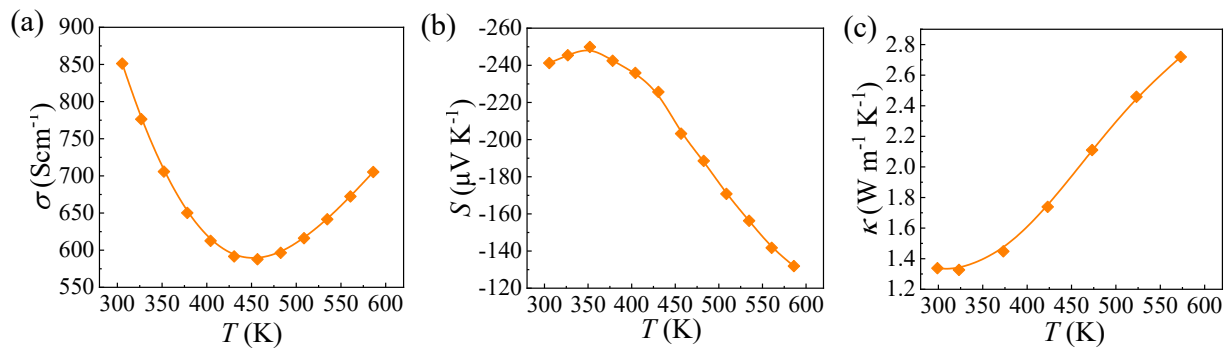


Fig. S9. Temperature dependence of thermoelectric performance for commercial n-type $\text{Bi}_2\text{Te}_{2.7}\text{Se}_{0.3}$. (a) Electrical conductivity, (b) Seebeck coefficient, and (c) total thermal conductivity.

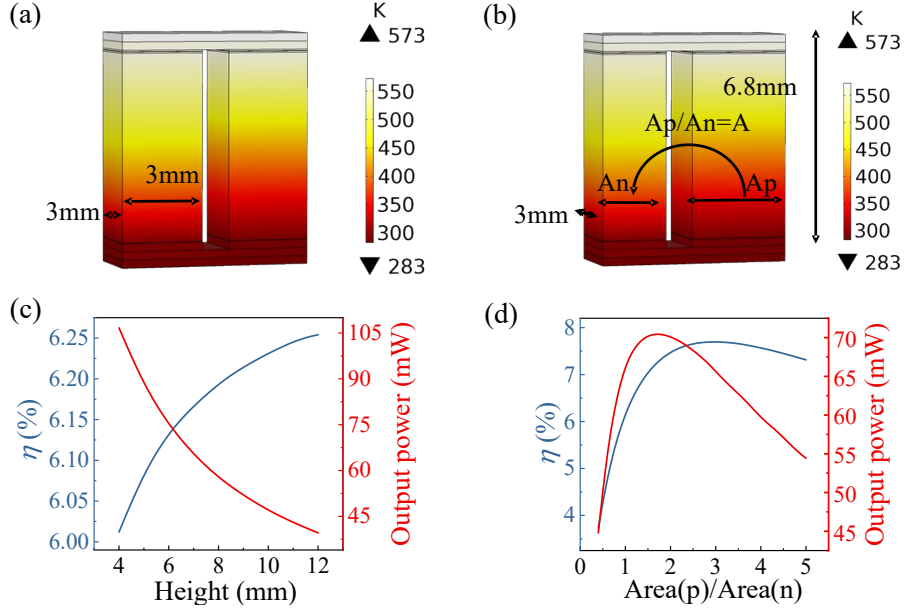


Fig. S10. Schematic diagrams of structural simulations with the high temperature end of 573 K and the low temperature end of 283 K: (a) for the arm length when the sectional areas of n-type and p-type thermoelectric arms are fixed as 3×3 mm, (b) for the sectional area ratios of the p-type thermal arm to the n-type when their total sectional area is summed as $6 \times 3 = 18$ mm². The simulated results of conversion efficiencies and output powers (c) under difference height of the thermoelectric arm and (d) under different sectional area ratios of the p-type thermal arm to the n-type by COMSOL.

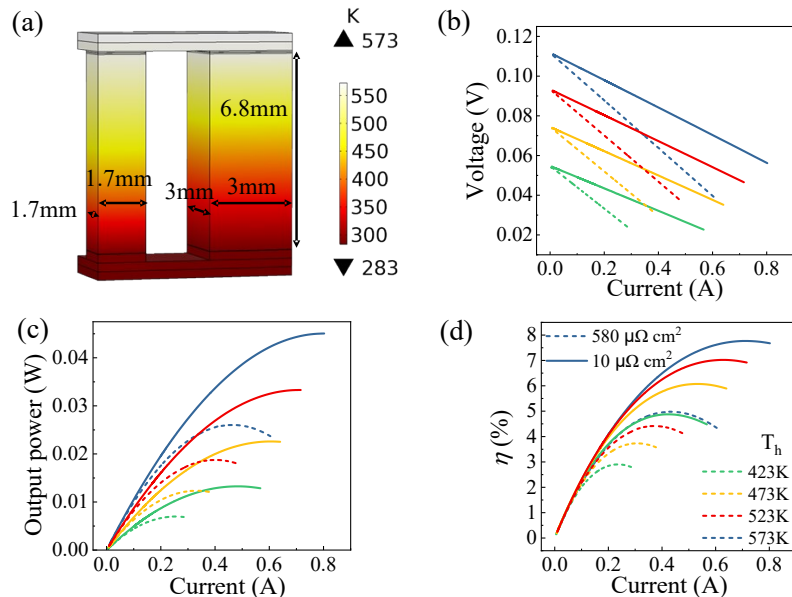


Fig. S11. (a) Schematic diagram of structural simulation for InTe-Bi₂Te₃ module. Current dependence of (b) voltage, (c) out power, and (d) conversion efficiency for InTe-Bi₂Te₃ module with different contact resistances.

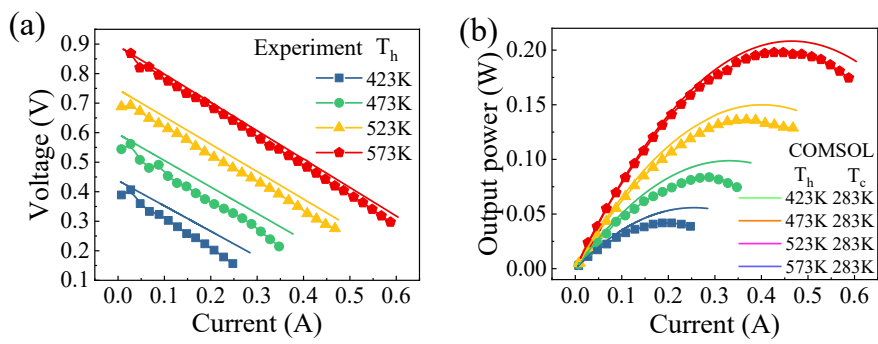


Fig. S12. Current dependence of (a) voltage and (b) out power for our InTe-Bi₂Te₃ module.

References

1. J. Y. W. Seto, *J. Appl. Phys.*, 1975, **46**, 5247-5254.
2. C. L. Hu, K. Y. Xia, C. G. Fu, X. B. Zhao and T. J. Zhu, *Energy Environ. Sci.*, 2022, **15**, 1406-1422.
3. J. J. Kuo, S. D. Kang, K. Imasato, H. Tamaki, S. Ohno, T. Kanno and G. J. Snyder, *Energy Environ. Sci.*, 2018, **11**, 429-434.
4. J. Bardeen and W. Shockley, *Phys. Rev.*, 1950, **80**, 72-80.
5. D. G. Cahill, S. K. Watson and R. O. Pohl, *Phys. Rev. B*, 1992, **46**, 6131-6140.
6. M. T. Agne, R. Hanus and G. J. Snyder, *Energy Environ. Sci.*, 2018, **11**, 609-616.
7. Y. Z. Pei, A. D. LaLonde, H. Wang, G. J. Snyder, *Energ. Environ. Sci.* 2012, **5**, 7963-7969.
8. M. K. Jana, K. Pal, U. V. Waghmare and K. Biswas, *Angew. Chem. Int. Ed.*, 2016, **55**, 7923-7927.
9. H. X. Zhu, B. Zhang, G. W. Wang, K. L. Peng, Y. C. Yan, Q. Zhang, X. D. Han, G. Y. Wang, X. Lu and X. Y. Zhou, *J. Mater. Chem. A*, 2019, **7**, 11690-11698.
10. H. X. Zhu, G. W. Wang, G. Y. Wang, X. Y. Zhou and X. Lu, *J. Alloys Compd.*, 2021, **869**, 159224-159229..
11. R. C. Huang, Y. Huang, B. Zhu, M. K. He, Z. H. Ge, L. W. Fu and J. Q. He, *J. Appl. Phys.*, 2019, **126**, 125108.
12. S. Misra, A. Léon, P. Levinský, J. Hejtmánek, B. Lenoir and C. Candolfi, *J. Mater. Chem. C*, 2021, **9**, 14490-14496.
13. S. Y. Back, H. Cho, Y. K. Kim, S. Byeon, H. Jin, K. Koumoto and J. S. Rhyee, *AIP Adv.*, 2018, **8**, 115227-115237.
14. S. S. Pan, H. Liu, Z. L. Li, L. You, S. N. Dai, J. Yang, K. Guo and J. Luo, *J. Alloys Compd.*, 2020, **813**, 152210-152216.
15. S. Misra, P. Levinský, A. Dauscher, G. Medjahdi, J. Hejtmánek, B. Malaman, G. J. Snyder, B. Lenoir and C. Candolfi, *J. Mater. Chem. C*, 2021, **9**, 5250-5260..
16. F. Li, X. Liu, N. Ma, L. Chen and L. M. Wu, *Angew. Chem. Int. Ed.*, 2022, **61**, e202208216.